Pleistocene volcanism along the margins of the Canal de Ballenas transform fault, Gulf of California

Arturo Martín-Barajas[1,*], Axel K. Schmitt[2], Bodo Weber[1], and Margarita López-Martínez[1]

[1] *Departamento de Geología, Centro de Investigación Científica y Educación Superior de Ensenada, Baja California, Mexico.*
[2] *Institute of Earth Sciences, Ruprecht-Karls-Universität, Heidelberg, Germany.*
*amartin@cicese.mx

ABSTRACT

Pleistocene subaerial volcanism along the margins of the Ballenas Channel, northern Gulf of California, is represented by two morphologically young dacite dome complexes exposed at the opposite edges of sheared continental crust: Isla Coronado in coastal Baja California, and the Lobera volcanic complex in west-central Isla Ángel de la Guarda. Single crystal zircon U-Pb crystallization ages of Coronado and Lobera volcanoes range between *ca.* 250 and 1000 ka, indicating maximum ages for the eruptions. Eruption ages are directly constrained by an $^{40}Ar/^{39}Ar$ whole-rock age of 692 ± 164 ka for one of the lava units in the Lobera volcanic complex. Trace elements in Pleistocene zircon indicate continental affinity, which supports radiogenic (Nd, Sr) isotopic data that were modeled using different mixing and AFC scenarios indicating a MORB-type primary magma with significant (~10–20 %) crustal assimilation involving tonalitic basement of the eastern Peninsular Ranges Batholith.

Keywords: Gulf of California; Ballenas fault; evolved volcanism; geochronology; geochemistry; Mexico.

RESUMEN

El volcanismo del Pleistoceno a lo largo de los márgenes del Canal de Ballenas, norte del Golfo de California, está representado por dos domos dacíticos que afloran en lados opuestos de la zona de cizalla continental: Isla Coronado en la costa de Baja California y el complejo volcánico La Lobera en la costa oeste de Isla Ángel de la Guarda. Las edades de cristalización obtenidas por el método U-Pb en circones individuales, varían entre ca. 250 y 1000 ka e indican la edad máxima de erupción. La edad de erupción está directamente acotada por una edad Ar-Ar en roca total de 692 ± 164 ka en uno de los flujos de lava en el complejo volcánico La Lobera. La composición de elementos traza en circones indica una afinidad continental, lo cual es consistente con datos isotópicos de Nd y Sr. Los datos isotópicos se modelaron utilizando diferentes escenarios de mezcla, asimilación y cristalización fraccionada (AFC) e indican un magma primario tipo MORB con asimilación cortical significativa (~10 a 20 %) del basamento tonalítico peninsular.

Palabras clave: Golfo de California; falla Canal de Ballenas; volcanismo diferenciado; geocronología; geoquímica; México.

INTRODUCTION

The Gulf of California hosts the trans-tensional domain of the Pacific-North America plate boundary (Fletcher *et al.*, 2014). This boundary is defined by lengthwise dominant transform faults that connect an *en-echelon* array of pull-apart basins at variable stages of crustal separation and sea-floor spreading (Figure 1). The maturity of the pull-apart basins and their interconnecting transform faults decreases north of the Guaymas basin where the Guaymas transform fault splays into several strike slip faults that shear continental crust (Lonsdale, 1989). The geological transition from mature oceanic spreading centers and transform faults in the southern Gulf of California to typically much smaller basins in the northern Gulf of California coincides with major oceanographic and faunal changes in the region of the so-called Midriff Islands which include Isla Ángel de la Guarda, San Esteban, and Tiburón (Figure 1).

Within the Ballenas channel, an ~80 km long submarine continental transform fault system separates the Baja California peninsula from Isla Ángel de la Guarda. The Ballenas Transform fault (BTF) juxtaposes continental crustal blocks of similar structure and composition along most of its length: on the east side, the continental block of Isla Ángel de la Guarda has become part of the North American plate, whereas the Baja California peninsula moves with the Pacific plate, with both blocks passing each other at a velocity of 47.3 ± 0.8 mm/yr (Plattner *et al.*, 2015). It further connects two young rift basins, the Lower Delfín basin to the north, and the more diffuse Ballenas and Salsipuedes basins in the south (Figure 1). The length of new oceanic crust is < 20 km for the Lower Delfín basin, where new crust is inferred to occupy a narrow rift with several submarine volcanoes located in the axial trough and over the faulted margins (Persaud *et al.*, 2003). The extent of new oceanic crust is likely smaller in the Salsipuedes basin (Figure 1), although multibeam bathymetry also depicts volcanoes in the southern Salsipuedes and the centrally located Ballenas basins (Plattner *et al.*, 2015). The seamounts in the Ballenas basin form a north-northeast alignment of small volcanoes that projects south onto Isla Coronado (ICO), locally also referred to as Isla Smith (Figure 2). This island is a 300 m-high dacite dome offshore the Main Gulf Escarpment where continental crustal rocks are down-faulted towards the basin. Another volcanic field occurs in the west central part of Isla Ángel de la Guarda, which shows a more pristine morphology compared to the regional volcanic deposits of Miocene age (Figure 2). This newly defined Lobera Volcanic Complex (LVC) is named after the eponymous seal colony (lobo marino) that permanently occupies the cliffy shore of the LVC.

To better understand the timing and origin of magmas in sheared and thinned transitional continental crust, we investigate volcanic rocks from ICO and the LVC on Isla Ángel de la Guarda. Their youthful, but not quite pristine morphology (*cf.* Isla San Luis; Paz-Moreno and Demant, 1999), is consistent with Pleistocene activity, but no radiometric age constraints have been reported so far. In this paper we present U-Pb zircon and Ar-Ar whole-rock geochronologic data to constrain magmatic differentiation and eruption ages, and report reconnaissance major and trace element geochemistry as well as Nd-Sr isotopic compositions of lavas to evaluate the source and composition of parental magmas in this important transitional part of Gulf of California rift zone.

TECTONIC AND GEOLOGIC FRAMEWORK

The BTF accommodates nearly all of the Pacific-North America plate motion in the northern Gulf of California, with less than ~10 % of plate motion occurring along the Tosco-Abreojos fault in the Pacific margin of Baja California (Plattner *et al.*, 2007). It connects two proto-oceanic pull-apart basins, the Lower Delfín in the north and

the Ballenas-Salsipuedes basins located in southeast end of the BTF (Figure 1). This transform fault developed in the late Pliocene when the Tiburón continental transform fault became inactive and the main plate boundary shifted west into the BTF, resulting in the capture of the continental block of Isla Ángel de la Guarda (Aragón-Arreola and Martín-Barajas, 2007; Martín-Barajas *et al.*, 2013).

Low-temperature thermochronology of crystalline rocks onshore the Ballenas transform margin in Baja California suggests that dextral shearing and uplift of the transform margin in Baja California occurred by ~1.8 Ma (Seiler *et al.*, 2009). Furthermore, correlation of distinctive volcanic deposits across the Ballenas Channel constrains dextral offset in the BTF between ~100 and 130 km (Stock *et al.*, 2009). This displacement is broadly consistent with the ~90 km length separation of continental crust in both the Upper and Lower Delfín basins based on interpretation of industry seismic profiles (Martín-Barajas *et al.*, 2013; Téllez-Velázquez, 2018).

Extension in the Lower and Upper Delfín basins is transferred to dextral shear in the BTF and has detached the continental block of Isla Ángel de la Guarda from the Baja California peninsula. Although the BTF concentrates most of the North America – Baja California relative motion, the capture of Isla Ángel de la Guarda is probably incomplete
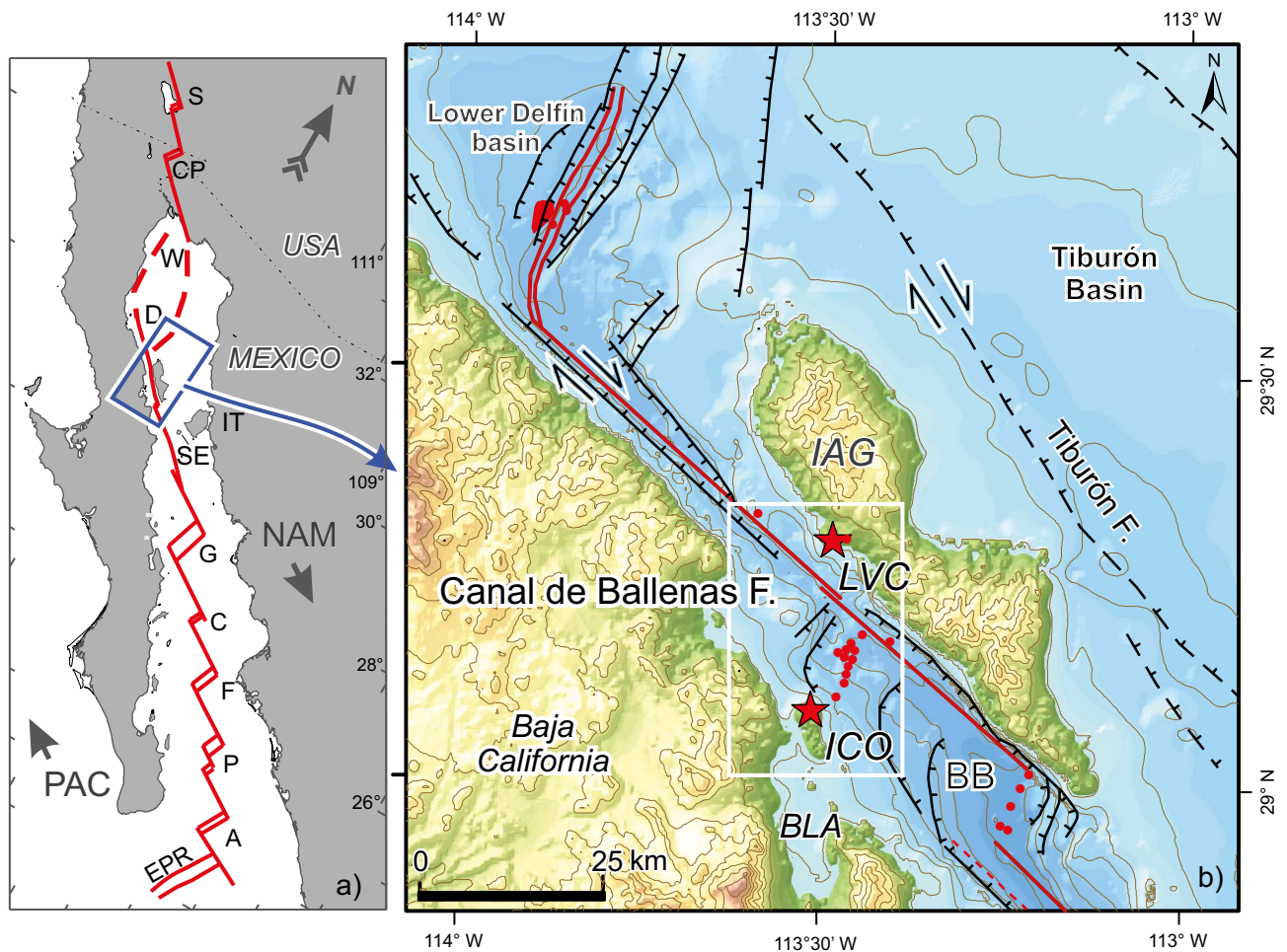

Figure 1. a). Simplified tectonic map of the Gulf of California rift zone with the Pacific (PAC) – North America (NAM) plate boundary (in red). Abbreviations for pull-apart basins (overview) S = Salton Trough, CP = Cerro Prieto, W = Wagner, D = Delfín, G = Guaymas, C = Carmen, F = Farallón, P = Pescador, A = Alarcón, EPR = East Pacific Rise. IT = Isla Tiburón, SE = Isla San Esteban. b). Bathymetry and topography map of the Canal de Ballenas Transform fault zone and the Lower Delfín basin at the northwest end. Red spots and stars are Plio-Pleistocene volcanoes. Major faults from Plattner *et al* (2015) and Martín-Barajas *et al.* (2013). Abbreviations (main map): IAG = Isla Ángel de la Guarda, ICO = Isla Coronado, BA = Bahía de los Ángeles, BB = Ballenas basin, TB = Tiburón basin. Bathymetry and topography is from the GEBCO_2021 Grid. Isobaths are 200 m contours.

as Quaternary deformation in the south part of Isla Ángel de la Guarda produces a north-northeast trend of normal and oblique faults (Higa *et al.*, 2022), and significant historic seismicity is reported east of the BTF (Castro *et al.*, 2017).

Magmatism in this young rift-transform system is ubiquitous, and submarine volcanoes are identified in high-resolution seismic profiles (Persaud *et al.*, 2003; Hurtado-Brito, 2012), and sea-beam bathymetry (Plattner *et al.*, 2015). Some of these submarine volcanoes are rhyolite and andesite pumice cones (Martín-Barajas *et al.*, 2008; Henyey and Bishop, 1973), and a seamount reported by Plattner *et al.* (2015) in the Ballenas basin is composed of basaltic lava (P. Lonsdale written comm.) (Figure 2). The ICO and LVC volcanoes may represent magmatic activity at the intersection between rift basins and transform faults under the influence of adjacent continental crust that is being actively sheared along the transform boundaries.

GEOCHEMISTRY AND GEOCHRONOLOGY METHODS

Whole rock geochemistry

Several kilograms of non-weathered rock were crushed and sieved, and ~250 grams of rock chips 2 to 5 mm in diameter where hand-picked and cleaned with deionized water in ultrasound bath, and then treated with HCl at 10 % concentration, and cleaned again in the ultrasound bath with deionized water. Rock chips were grounded in a Tungsten
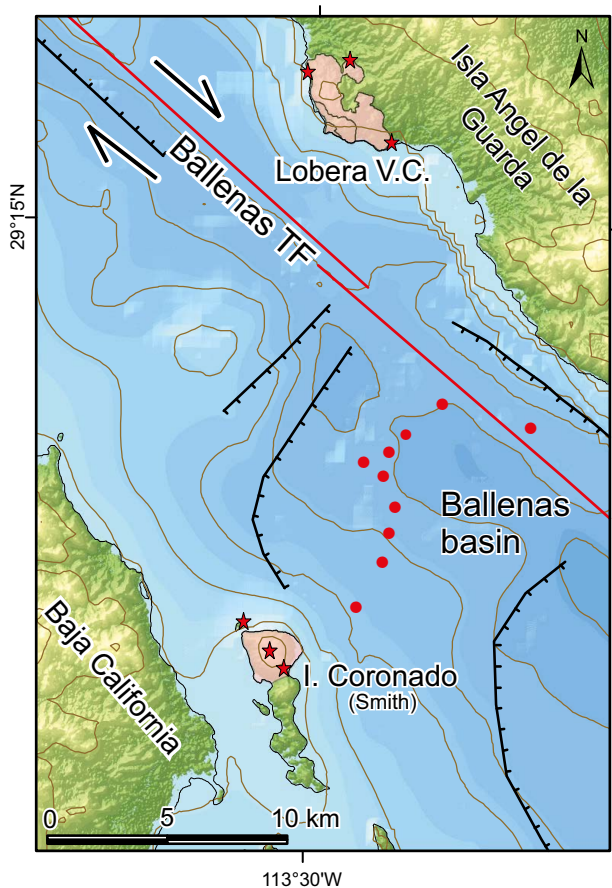

Figure 2. Bathymetry and structural map of the Ballenas basin. Sample locations (red stars) and submarine volcanic mounts (red circles) reported by Plattner *et al* (2015) are shown. The Lobera volcanic complex (LVC) and Isla Coronado are Pleistocene volcanic events at the margins of the sheared continental crust.

carbide ring mill into a powder of <60 μm. Major oxide and trace element composition was obtained by XRF and ICP-MS, respectively at the Peter Hooper GeoAnalytical Laboratory at Washington State University (WSU) in Pullman, Washington (Table 1). Analytical procedures and uncertainties for major oxides and trace elements using XRF are described in Hooper *et al.* (1993). Precision for the ICP-MS analysis is typically better than 5 % (RSD) for the rare earth elements (REE) and 10 % for the remaining trace elements (see Technical notes of the WSU GeoAnalytical Lab web page).

Sm-Nd-Sr isotope geochemistry

Chemical preparation for whole-rock isotope analysis (Table 2) was performed in PicoTrace® clean lab facilities at Departamento de Geología, Centro de Investigación Científica y de Educación Superior de Ensenada (CICESE) in the state of Baja California (Mexico). About 100 mg of powdered rock sample was weighed together with ^{84}Sr-^{145}Nd-^{149}Sm tracer solutions into Teflon bombs of a Picotrace DAS® pressure digestion system and dissolved in a mixture of HF, HNO_3 and $HClO_4$ at *ca.* 165 °C. After evaporation and sample-spike equilibration, Sm, Nd, and Sr element separation was achieved in two steps, first with quartz-glass columns filled with DOWEX AG 50W-X8 resin to separate Sr and REE and then with Ln-Spec® resin to separate Nd (Weber *et al.*, 2012). Samarium, Nd and Sr isotopes were analyzed by thermal ionization mass spectrometry (TIMS). The LVC samples were analyzed with a Thermo Triton Plus® installed at Laboratorio Universitario de Geología Isotópica (LUGIS) of the Universidad Nacional Autónoma de México (UNAM), Mexico City (*e.g.* Weber *et al.*, 2012), whereas ICO samples were measured with a Nu Instruments equipment (Nu-TIMS) at CICESE (*e.g.,* Cisneros de León *et al.*, 2019). Correction for mass bias for Sr and Nd was achieved by normalizing to ^{86}Sr/^{88}Sr = 0.1194 and ^{146}Nd/^{144}Nd = 0.7219, respectively. Neodymium standards JNdi-1 and La Jolla analyzed in the same run as the unknowns yielded ^{143}Nd/^{144}Nd = 0.512106 ± 4 (2 s.e.) and 0.511831 ± 4, respectively. Strontium NIST 987 standard yielded ^{87}Sr/^{86}Sr = 0.710258 ± 7 (2 s.e.).

U-Pb and U-Th zircon geochronology and trace element analysis

The ICO and LVC rocks are zircon poor, and >60 kg of rock had to be processed to extract ~20 zircon crystals per sample. Crystals were handpicked and mounted in epoxy, sectioned and polished, and imaged using a cathodoluminescence detector. Secondary ionization mass spectrometry analyses of ICO and LVC zircon crystals were carried out on the UCLA CAMECA ims 1270 and the Heidelberg University CAMECA ims 1280, respectively, using methods for U-Pb and U-Th geochronology described in Schmitt *et al.* (2003) and Schmitt *et al.* (2010). All U-Pb ages are reported against AS3 reference zircon (1099 Ma), and analytical accuracy was monitored through analysis of 91500 reference zircon for which an age of 1082 ± 18 Ma (n = 6; mean square of weighted deviates MSWD = 0.46) was obtained. Radiogenic ^{206}Pb/^{238}U and corresponding ages were determined from the concordia intercept of a linear regression in a Tera Wasserburg concordia diagram with a fixed y-axis intercept corresponding to ^{207}Pb/^{206}Pb = 0.828 (Stacey-Kramers model Pb for 0 ka; Stacey-Kramers, 1975); only for xenocrystic zircon >20 Ma, ^{204}Pb-corrected ^{206}Pb/^{238}U or ^{207}Pb/^{206}Pb (>500 Ma) ages are reported using corresponding Stacey-Kramers model Pb compositions. The U-Th relative sensitivity factor (RSF) was calibrated following Reid and Coath (1997) and monitored by analyzing AS3 reference zircon for which a secular equilibrium value of (^{230}Th)/(^{238}U) = 1.004 ± 0.036 Ma (n = 5; MSWD = 0.01) was determined. An isochron age was fitted through the data to determine the U-Th age, excluding xenocrystic (secular equilibrium) crystals identified by U-Pb dating. Trace elements were analyzed by SIMS on the instruments stated above with analytical procedures described in

Table 1. Major oxides (wt%) and trace elements (ppm) content in lavas from Isla Coronado (ICO) and Lovera volcanic complex (LVC) in Isla Ángel de la Guarda.

Sample ID	IAG07-40	IAG07-38	ICO08-1	ICO08-2	ICO08-3
Area/Unit	Lobera Qv2	Lobera Qv1	I Coronado	I Coronado	I Coronado
Lat N	29° 18' 40.13"	29° 18' 36.23"	29° 5' 16.62"	29° 5' 0.6"	29° 5' 49.62"
Lon W	113° 29' 14.2"	113° 30' 20.1"	113° 30' 49.8"	113° 30' 43.3"	113° 31' 46.7"
Lithology	D	D	D	D	D
SiO_2	64.33	63.74	67.9	68.73	67.37
TiO_2	0.86	1.03	0.47	0.47	0.48
Al_2O_3	15.74	16.23	15.55	15.64	14.95
FeO*	4.85	5.25	3.48	3.39	3.25
MnO	0.09	0.09	0.07	0.07	0.07
MgO	1.43	1.74	1.4	1.19	1.09
CaO	4.35	4.79	4.09	3.62	3.59
Na_2O	4.69	4.59	4.7	4.76	4.72
K_2O	1.46	1.48	1.58	1.67	1.91
P_2O_5	0.25	0.23	0.14	0.14	0.14
Sum	98.05	99.19	99.36	99.69	97.59
LOI (%)	0.83	-0.15	0.08	0	0.34
Trace elements ICP-MS					
La	16.13	14.61	14.76	15.24	16.77
Ce	35.58	32.77	31.44	32.71	35.86
Pr	4.8	4.43	4.08	4.26	4.65
Nd	20.04	18.77	16.93	17.58	19.26
Sm	4.97	4.73	3.93	4.11	4.49
Eu	1.34	1.34	1.02	1.08	1.13
Gd	5.03	4.75	3.88	4.2	4.55
Tb	0.85	0.82	0.66	0.7	0.75
Dy	5.1	5.09	4.03	4.32	4.79
Ho	1.08	1.05	0.83	0.9	0.99
Er	2.96	2.87	2.26	2.47	2.76
Tm	0.44	0.42	0.34	0.36	0.41
Yb	2.68	2.58	2.13	2.29	2.51
Lu	0.42	0.42	0.34	0.37	0.4
Ba	688.54	575.53	752.74	676.19	693.51
Th	3.95	3.32	3.11	3.34	3.98
Nb	5.6	5.43	4.67	4.94	5.31
Y	27.82	27.1	21.89	23.06	25.65
Hf	4.4	4.4	4.38	4.62	4.91
Ta	0.43	0.42	0.34	0.36	0.4
U	1.38	1.01	1.04	1.15	1.35
Pb	8.84	7.58	7.75	8.31	8.8
Rb	41.93	35.13	34.6	38.9	45.8
Cs	1.8	1.51	1.17	1	1.7
Sr	410.13	421.55	472.91	466.13	433.95
Sc	10.62	12.09	8.2	8.3	8.1
Zr	164.08	161.87	158	169	182

Major oxides and trace elements analyzed at Geoanalytical Laboratory Washington State University by FRX and ICP-MS respectively. FeO* = total Fe.

Schmitt and Vazquez (2017). NIST SRM 610 glass with trace elemental abundances of Pearce *et al.* (1997) was used to determine RSF values for high energy ions (-100 eV offset). 91500 reference zircon was analyzed in the same session for monitor accuracy, and only minor deviations from nominal values (Wiedenbeck *et al.*, 2004 for Hf, REE, and U; Szymanowski *et al.*, 2018 for Ti) were observed, which for the plotted elements are +3.7 % (Eu/Eu*), +2.4 % (Hf), +4.7 % (Ti), +3.4 % (Y), +2.8 % (Yb), and +14.7 % (U).

Ar-Ar geochronology

Isotopic dating by $^{40}Ar/^{39}Ar$ was performed in the Geochronology Laboratory at CICESE using a VG5400 mass spectrometer and laser step-heating experiments. One whole-rock sample of the LVC was ground (355–710 μm), washed with de-ionized water, and cleaned under a stereomicroscope to eliminate phenocrysts and altered material. The samples were irradiated in the nuclear reactor at the University of McMaster in Hamilton, Canada, for 10 hours at 2 MW/hour. Samples FCT-2 (28.201 ± 0.046 Ma; Kuiper et al, 2008), and TCR-2 (24.34 ± 0.28 Ma; Renne *et al.*, 1998) were used as internal standards (see Supplementary Material). The Ar extraction line include a laser beam connected in line with the mass spectrometer. Aliquots of atmospheric composition were analyzed at the end of each day to correct for discrimination effects of the mass spectrometer. Argon isotopes were corrected for radioactive decay of ^{37}Ar and ^{39}Ar. Corrections

Table 2. Sr, Sm-Nd isotope data.

Sample ID	Field description	Unit	Sr (ppm)	⁸⁷Sr/⁸⁶Sr	2 s.e. ×10⁶	Sm (ppm)	Nd (ppm)	¹⁴⁷Sm/¹⁴⁴Nd	¹⁴³Nd/¹⁴⁴Nd	2 s.e. ×10⁶	εNd (a)
IAG07-40	Dark grey, blocky lava at the top of Qv2, aphanitic to microporphiritic, <200 % of plagioclase and pyroxene microcrystals. Common lithic inclusions and phyric aglomerates.	Qv2	413	**0.704341**	10	4.43	19.2	0.1494	**0.512822**	4	**3.75**
IAG07-38	Black glassy lava flow with columnar structure and basal brecchia Qv1. Dark grey color towards the upper part of the flow (devitrification?) and pervasive diaclases. Plagioclase and pyroxene microphenocrysts.	Qv1	425	**0.704133**	13	4.68	20.1	0.1513	**0.512842**	3	**4.14**
ICO-08-1	Dacite dome composed of two individual flows with reddish basal and somital brecchias. Dark grey aphanitic lava <1-2 % plagioclase microphenocrysts. Sample ICO08-1 was collected at the top of the upper lava flow.	Qd1	462	**0.704164**	7	3.68	16.8	0.1321	**0.512734**	3	**2.02**
ICO-08-3	Dark grey dacite lava collected in the northern islet separated ~25 meters from the main dome at ICO.	Qd2	418	**0.704169**	8	4.16	19.0	0.1326	**0.512756**	3	**2.46**

(a) Epsilon Nd (εNd) is the deviation of ¹⁴³Nd/¹⁴⁴Nd of the sample relative to the chondritic uniform reservoir (CHUR) times 10000. CHUR ¹⁴³Nd/¹⁴⁴Nd = 0.512630 (after Bouvier *et al.* 2008).

for interfering reactions of isotopes of Ca and K were applied using the factors reported by Bottomley and York (1976) for the McMaster reactor. The Cl interference on ³⁶Ar suggested by Roddick (1983) was also corrected, and the constants recommended by Steiger and Jäger (1977) were applied in all the calculations. The samples were laser-heated between 0.3 and 7.0 W. The integrated age was calculated by abundance addition for each fraction, and the error in the integrated age includes the uncertainty due to factor J; all errors are reported at 1 σ level (Table S1 in the Supplementary Material).

RESULTS

Lobera Volcanic Complex (LVC)

We conducted field reconnaissance and satellite spectral analysis on EO-1 data and Google Earth images of the LVC in the western-central part of Isla Ángel de la Guarda (Figure 3). LVC is a composite lava dome complex with three main lava units, the lower lava unit (Qv1) is exposed at the northwest cliffy shore (sample IAG07-38; supplementary Figure S2), but its vent location is obscured. The eroded cliff indicates
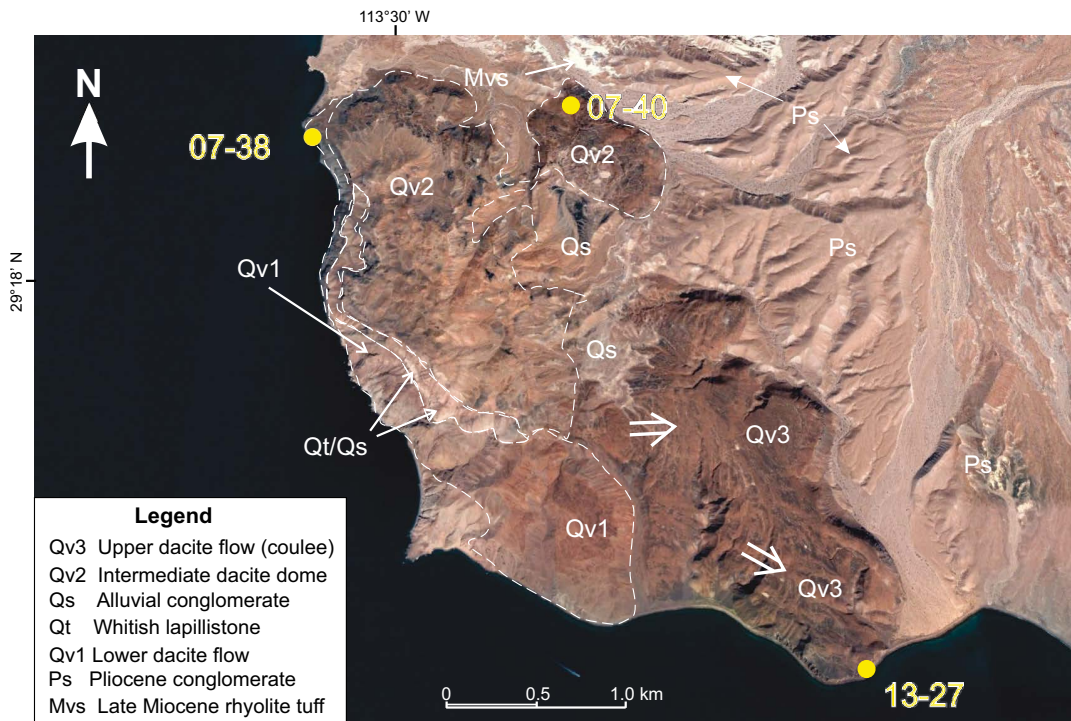

Figure 3. Google Earth image of the Lobera Volcanic Complex (LVC) with major map units and sample locations. Map units were defined from satellite spectral images (see Figure S1 in the Supplementary Material), and field reconnaissance.

this lava flow is at least 20–30 m-thick and displays ramp structures and columnar jointing. The top of Qv1 is brecciated and overlain by whitish pyroclastic deposits ranging a few meters in thickness (Qt in Figure 3). Pumice lapilli in this deposit are reworked towards the top and grade upwards into a ~15–20 m-thick conglomerate covered by the uppermost lava flow unit (Qv3).

The two younger lava units Qv2 and Qv3 crop out along the S-SE and NE flanks of LVC (Figure 3). The largest and morphologically youngest flow is a ~2 km long coulee, displaying arcuate pressure-ridges that indicate E-SE directed transport (Figure 3). An isolated lobe in the NE corner of the volcanic complex displays a circular ridge crest nearly 200 m in diameter (Qv2), which suggests a local vent or alternatively, this lobe could be part of a larger lava flow of intermediate age between the lower and upper lava units.

All three LVC lava units have similar mineral composition although they display textural differences. The lower flow (Qv1) is composed of a dark grey, aphanitic glassy lava, with <1 % plagioclase and pyroxene microphenocryst <1.5 mm long (see photomicrographs in the Supplementary Material). The plagioclase microlites are commonly aligned within the glassy matrix, and glomerophyric plagioclase and pyroxene are common. Lava units Qv2 and Qv3 are dark grey to black with an aphanitic to microporphyritic texture. Plagioclase microlites within the glassy matrix define a hypohyaline flow texture. In this matrix, agglomerates of plagioclase (andesine)-orthopyroxene phenocrysts and opaque minerals along with zoned plagioclase microphenocrysts are common.

Isla Coronado (ICO)

The ICO comprises a ~300 meter-high dacite dome located in the north end of the island (Figure 4), situated north of Bahía de los Ángeles (BLA in Figure 1b) This lava dome overlies a low relief crystal-line basement composed of Mesozoic granitic rocks and hornblende schist of presumably Paleozoic age. The lava dome includes two cooling units (ICO08-1 and ICO08-2) separated by a flow breccia, which also comprises most of the small islet near the northern tip of ICO (*e.g.*, sample ICO08-3)

The ICO lavas are dominantly hypohyaline to felsitic in texture with common glomerophyric plagioclase, pyroxene, and rare hornblende. Glomerophyric plagioclase is commonly euhedral and up to 1.5 mm in diameter; it displays oscillatory zonation and complex twinning. Plagioclase microlites are euhedral to subhedral and commonly associated with disseminated orthopyroxene and opaque minerals.

Major oxide and trace elements

Major oxide geochemistry in both ICO and LVC indicates dacitic composition of lavas (Figure 5a), although ICO samples are high-silica dacite compared to LVC lavas. The higher differentiation of ICO lavas is also reflected in lower content of MgO, TiO_2 and FeO_t, and higher K_2O (Table 1). Rare Earth elements display similar patterns in both ICO and LVC samples (Figure 5b), with a slightly higher LREE fractionation and Eu depletion in ICO lavas (La_n/Yb_n 3.75–3.91) compared to LVC dacite (La_n/Yb_n 3.20–3.39).

Sr and Sm-Nd isotopes of whole rock samples

Two ICO lava samples have within errors identical $^{87}Sr/^{86}Sr$ ratios of 0.704164 and 0.704169, slightly below the bulk earth and similar Nd isotope ratios yielding εNd values of +2.0 and +2.5, indicating a slightly depleted source (Table 2). Comparatively low $^{147}Sm/^{144}Nd$ ratios of 0.1321 and 0.1326 reflect the fractionated character of these high-
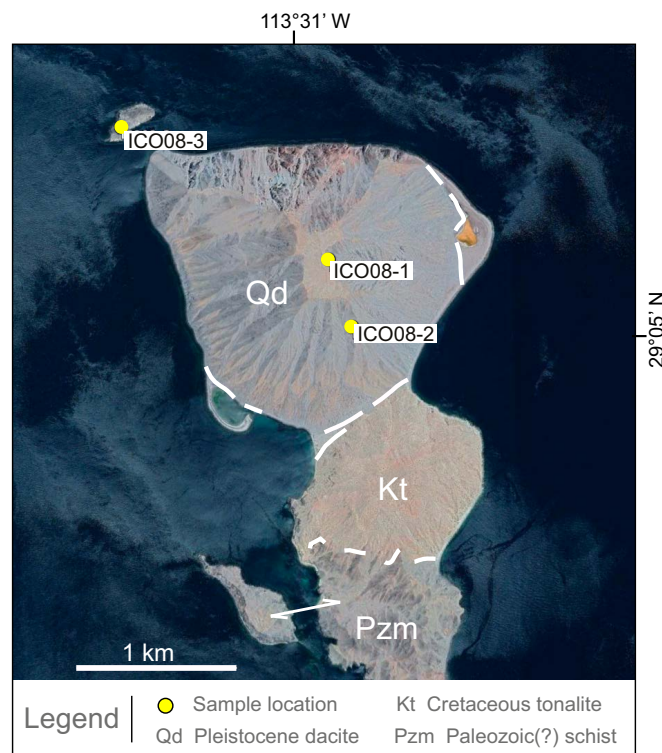

Figure 4. Google Earth image of Isla Coronado (Smith). The dacite dome is ±300 m high and erupted over granitic and metamorphic continental crust.
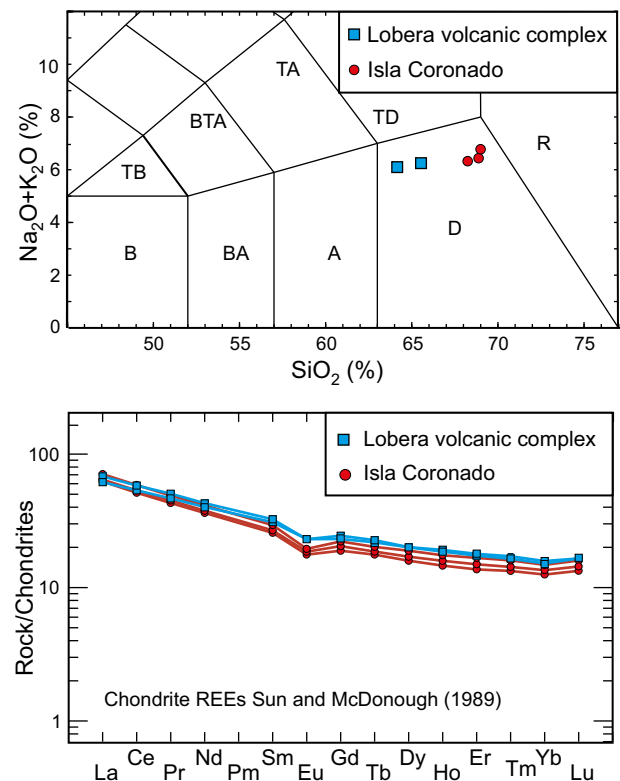

Figure 5. a) Total alkalis vs silica plot (from Le Bas *et al.*, 1986) with ICO and LVC samples analyzed for major oxide and trace elements geochemistry. b) Chondrite-normalized REE diagrams of selected samples from LVC (Isla Ángel de la Guarda) and Isla Coronado (ICO).

silica lavas. The LVC lavas display higher $^{147}Sm/^{144}Nd$ of 0.1494 and 0.1513, which is also consistent with their lower silica content. More radiogenic Nd isotope compositions, yielding εNd values of +3.8 and +4.1 suggest a larger component from the depleted mantle source in LVC dacites compared to ICO lavas. Strontium isotopes, however, do not reflect this tendency for the LVC samples. Their $^{87}Sr/^{86}Sr$ are either insignificantly lower (IAG07-38 = 0.704133) or higher (IAG07-40 = 0.704341) than ICO lavas, indicating some secondary process affecting Sr isotopes like hydrothermal processes or magma contamination with carbonates.

Geochronology and zircon trace elements

Two U-Pb and one Ar-Ar ages were determined for lava flows from the LVC. The Ar-Ar whole-rock analysis obtained from one sample of Qv2 lava of LVC comprises two experiments that yielded overlapping ages for the high-temperature release steps which average 692 ± 164 ka (n = 10; MSWD = 1.0) (Figure 6).

Due to large error obtained in the Ar-Ar whole rock analysis we processed a larger amount of rock in search of young zircon crystals. In spite of the low zircon yield, we obtained U-Pb crystallization ages from Qv1 and Qv3. The stratigraphically lowermost sample IAG07-39

(Qv1) yielded 9 zircon crystals with mostly mid-Miocene ages and one Cretaceous age (Figure 7a). Only two crystals (analyzed in triplicate) yielded a homogeneously Quaternary date with an error-weighted average of 1016 ± 60 ka (n = 6; MSWD = 1.50). The overlying lava flow Qv3 yielded 17 zircon crystals, but only one of Quaternary age (Figure 7b). This crystal was analyzed in triplicate, and a consistent error-weighted average of 358 ± 60 ka (n = 3; MSWD = 1.26) was obtained. Xenocrysts range in age from *ca.* 6.9 to 1013 Ma, with clusters in the Miocene (n = 3) and the Cretaceous (n = 6).

About 20 zircon crystals were separated for ICO dacite lavas, with 10 crystals yielding Quaternary ages (Figure 7c). The concordia intercept age of 247 ± 14 ka (n = 10; MSWD = 0.67) suggested a sufficiently young age for disequilibrium dating $(^{230}Th)/(^{238}U)$, and therefore the same crystals (along with xenocrysts for reference) were re-analyzed. An isochron age of 236 +156/-62 ka (n = 10; MSWD = 2.50) confirmed the $^{206}Pb/^{238}U$ concordia intercept age; because of the larger uncertainties of the U-Th age, however, we refer to the more precise U-Pb age in the subsequent discussion.

Trace elements in young zircons indicate a continental affinity (Figure 8). Quaternary zircon crystals from LVC have moderate U abundances (180–520 ppm) and U/Yb (0.19–0.48) *vs.* Hf (8090–9630 ppm) that fall within the field of continental zircon. Similarly, ICO zircon trace elements display elevated U abundances (810–2890 ppm) and U/Yb (0.94–2.1) at Hf abundances that mostly overlap those of LVC zircon (5180–9020 ppm) and that also fall within the continental field in zircon trace element discrimination diagrams (Figure 8).

DISCUSSION

Radiometric ages for LVC and ICO reveal Pleistocene evolved magmatism along the onshore margins of the Ballenas basin. Activity in the LVC appears to be older, with zircon ages (representing maximum eruption ages) in the lower Pleistocene. A stratigraphically consistent younger age was determined for zircon from the upper lava flow (Qv3), which is concluded to be of mid Pleistocene age. The lava flow Qv2 located in the northeastern part of the complex is intermediate in age between both lava flows dated using zircon separates, and yielded a $^{40}Ar/^{39}Ar$ whole rock age of 692 ± 164 ky (Figure 6) that is consistent with its intermediate stratigraphic position in the LVC.

Zircon ages for ICO, again interpreted as maximum eruption ages, postdate LVC zircon, and suggest activity at or after *ca.* 250 ka (Figure 7c and 7d), also during the mid-Pleistocene.

To further elucidate the age significance of zircon in these lavas, zircon trace element geochemistry is compared to whole rock compositions via published zircon-melt partition coefficients (table 5 in Sano *et al.*, 2002) (Figure 9). Because zircon saturates early in metaluminous melts, and the investigated rocks are crystal-poor, melt compositions may be reasonably well approximated by whole-rock compositional data. Thus, the comparison between predicted melt compositions (using measured zircon REE abundances divided by zircon-melt partition coefficients that range from 0.00046 for La to 325 for Lu, Sano *et al.*, 2002) and actual whole rock data is a first-order assessment whether zircon is in equilibrium with its host rock. Although the calculated range of REE from LVC zircon is wider than observed whole rock compositions (Figure 9b), they broadly overlap, some deviations for La and Ce notwithstanding. Both elements, however, are difficult to model as La is only present in very small amount in zircon, and Ce partitioning is redox dependent so that the values from Sano *et al.* (2002) may not be adequate for LVC zircon-melt equilibria. Nonetheless, the REE models of Figure 9b suggest that zircon from LVC crystallized from a melt similar to the whole rock compositions. Zircon genetic
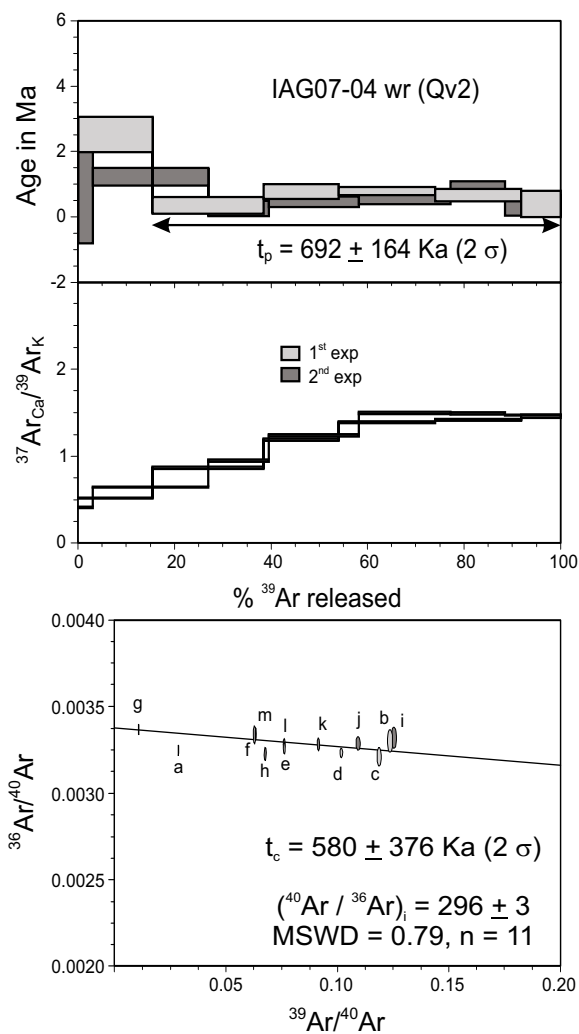

Figure 6. Ar-Ar stepwise heating diagram for two runs of a whole-rock sample IAG07-40 from Qv2 in the northeastern lava of the LVC. Plateau age for the high temperature steps is indicated using steps 2–6 for 1st experiment.
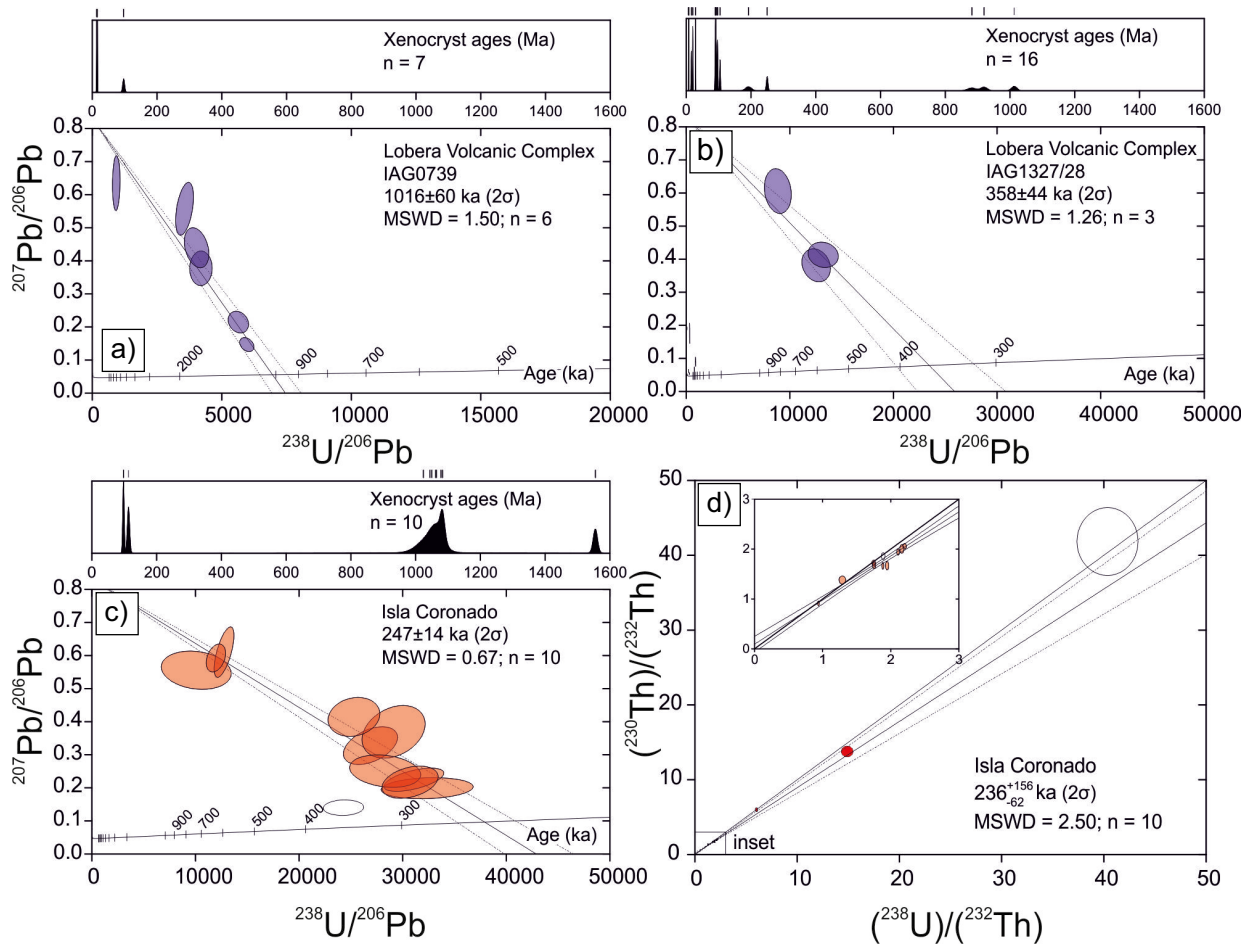
Figure 7. U-Pb and U-Th zircon geochronology results. U-Pb data are plotted uncorrected for common Pb with a linear regression fixed at common $^{207}Pb/^{206}Pb = 0.828$ where the radiogenic component and age is determined from the lower Concordia intercept. U-Th data are shown in an equiline diagram where isotopic activities are indicated by parentheses. The age is determined from the slope of the isochron defined by zircon with young U-Pb ages. Open symbols are omitted from regression.

classification diagrams (Grimes *et al.*, 2007) also indicate a larger crustal input into LVC zircon-crystallizing melts compared to those for Pleistocene volcanoes in the northern Gulf of California (Figure 8) (Schmitt *et al.*, 2013).

In contrast to LVC zircon, trace element abundances in ICO zircon are higher, suggesting that they crystallized from a more evolved melt (Figure 9a). This is also underscored by a pronounced negative Eu anomaly displayed by ICO zircon. Calculated melt compositions in ICO samples (see above) are significantly higher in REE (except Eu) than REE measured in whole rock samples (Figure 9b), again disregarding La and Ce for the reasons stated above. The mismatch between modelled and actual whole rock (melt) compositions implies that ICO zircon crystallized from a significantly more evolved melt than the dacitic host lava. In the light of the higher U/Yb of ICO zircon compared to LVC (*e.g.* Figure 8), a stronger crustal input into the zircon-crystallizing melt is also invoked for ICO. This is supported by whole rock radiogenic isotope data (Table 2) discussed below.

Magmatism associated with the Ballenas continental transform faults may results from decompression melting of the upper mantle in regions where oblique rifting generates trans-tensional domains at right steepened strike-slip faults. Similarly, volcanic products in the western margin of the Cerro Prieto and Wagner pull-apart basin are commonly evolved, reflecting protracted ascent and residence times within
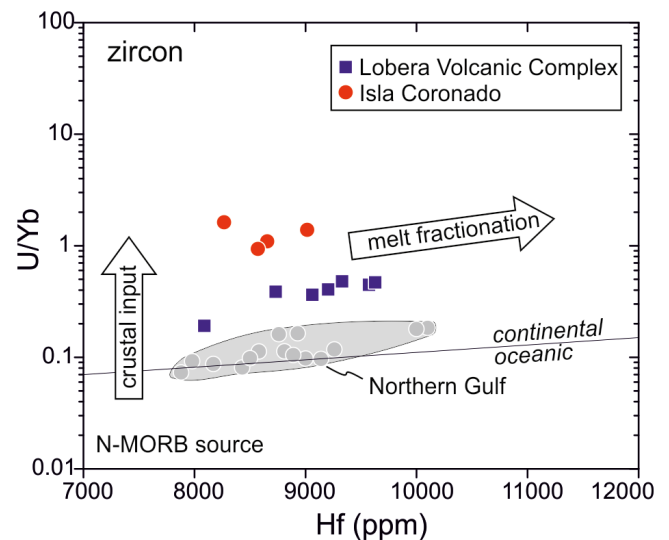

Figure 8. Zircon trace element classification diagram after Grimes *et al.* (2007). Data for northern Gulf zircons from Schmitt *et al.* (2013) shown for comparison.
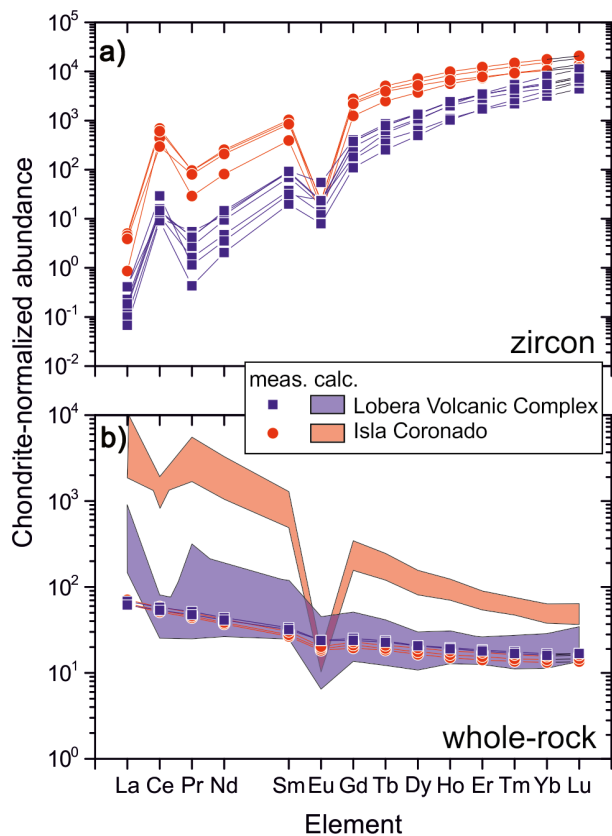
Figure 9. Chondrite-normalized rare earth element (REE) diagrams for (a) zircon and (b) whole rock along with calculated melt compositions that are expected to be in equilibrium with zircon. Calculations use literature zircon-melt partitioning coefficients (Sano *et al.*, 2002). With the exception of La (difficult to analyze due to extremely low abundances in zircon) and Ce (with a redox-sensitive partitioning coefficient), calculated melts agree with observed whole rock compositions for LVC, whereas ICO zircon trace elements reveal crystallization from much more evolved melts than indicated by whole rock compositions.

continental crust and sediments, and differentiation of basaltic melts occurring via crystal fractionation and/or crustal assimilation (Schmitt *et al.*, 2013; Herzig and Jacobs, 1994). In this work assimilation-fractional crystallization (AFC) models were set up for a consistency check for a magma genetic scenario where mid ocean ridge basalt (MORB) as a parental magma interacted with continental basement (Figure 10). Calculations were based on simple binary mixing, the classical AFC algorithm in De Paolo (1981), and energy-constrained (EC) AFC models (Spera and Bohrson, 2001). More sophisticated models accounting for recharge and temperature-dependent changes in the crystallizing mineral assemblage and partitioning coefficients (*cf.* Heinonen *et al.*, 2021) were not attempted as these would require additional constraints that are currently unavailable. The parental MORB composition was taken from submarine basalts of the Alarcón Basin in the southern Gulf of California (Castillo *et al.*, 2002). Crustal assimilate as indicated from regional geological mapping include Tertiary volcanic rocks that are abundant on the surface, Mesozoic tonalites belonging to the eastern Peninsular Ranges Batholith suite, as well as metamorphic rocks including hornblende schists.

Pre-Quaternary zircon encountered in LVC samples is dominated by Tertiary ages (48 %), with Cretaceous ages between 105 and 90 Ma being the second largest population (30 %). In ICO samples, Cretaceous ages between 113 and 98 Ma were also found, but the remainder

is Proterozoic with the largest population of Proterozoic xenocryst zircon dated around ~1100 Ma (Figure 7c). In the absence of direct constraints on crustal compositions, we thus use eastern Peninsular Ranges Batholith Nd-Sr compositions as a crustal contaminant because (1) it matches a significant proportion of detrital ages, (2) such rocks presumably constitute a significant portion of the mid to lower continental crust of the Baja California peninsula, and they are more likely to become assimilated than upper crustal Tertiary volcanic rocks, and (3) the eastern Peninsular Ranges Batholith is itself a mantle-crustal hybrid which sampled and integrated pre-batholithic basement for which there are no outcrops in the direct vicinity.

Model curves for mixing and AFC scenarios in the εNd *vs.* $^{87}Sr/^{86}Sr$ space plot closely to the ICO data (Figure 10), and also match compositions for lava from Roca Consag, a volcanic island in the Wagner basin of the northernmost Gulf of California (Schmitt *et al.*, 2013). LVC data are identical in εNd to Roca Consag, but displaced to higher $^{87}Sr/^{86}Sr$. Similar sub horizontal trends are displayed by submarine lavas from the Lower Delfín Basin (Martín-Barajas *et al.*, 2008) and also known for volcanic rocks from geothermally active onshore basins of the northern Gulf of California rift (Schmitt *et al.*, 2013). They are interpreted as results of hydrothermal alteration, and therefore high-$^{87}Sr/^{86}Sr$ data are considered unreliable as indicators of magmatic compositions. It is therefore concluded that binary mixing and/or AFC involving MORB magmas and tonalitic basement can explain the compositions of the Ballenas Channel evolved volcanic rocks. The amount of crustal material added to the erupted magma, as indicated by the different models, is at most ~10–20 %, within the range of other Pleistocene volcanic rocks from the northern Gulf of California magmatic province (Schmitt *et al.*, 2013; Figure 10). A slightly larger crustal input into the ICO source relative to LVC is consistent with findings from zircon and whole-rock geochemistry.

CONCLUSIONS

Two sets of volcanic vents have developed during the Pleistocene on opposite sides of the Ballenas transform fault within the Midriff section of the Gulf of California. These vents form Isla Coronado (ICO) at the southwestern terminus of the Ballenas basin, and the Lobera Volcanic Complex (LVC) on Isla Ángel de la Guarda on the northeastern end. Both volcanoes are located on the edge of sheared crystalline basement comprising tonalite and hornblende schists, which are overlain by Miocene volcanic rocks. This crustal segment has been previously thinned in dilatational domains of the transform fault system such as the Ballenas basin, which comprises several submarine volcanic knolls (Plattner *et al.*, 2015). Zircon crystallization ages of the ICO and LVC volcanoes range between *ca.* 250 and 1000 ka. Exact eruption ages are unknown, except for a *ca.* 700 ka $^{40}Ar/^{39}Ar$ age for a lava unit (Qv2) in the northeastern part of the LVC, but younger than the zircon crystallization ages. The young morphology of unit Qv3 in the southeastern LVC is consistent with the youngest zircon ages detected for the LVC of *ca.* 360 ka. The ICO eruption postdates *ca.* 250 ka as indicated by zircon crystallization ages. Radiogenic (Nd, Sr) isotopes suggest a MORB-type primary magma with significant (~10–20 %) crustal assimilation involving tonalitic basement of the eastern Peninsular Ranges Batholith.

SUPPLEMENTARY MATERIAL

Supporting supplementary material can be found in the html version of this paper at the RMCG website: www.rmcg.unam.mx.

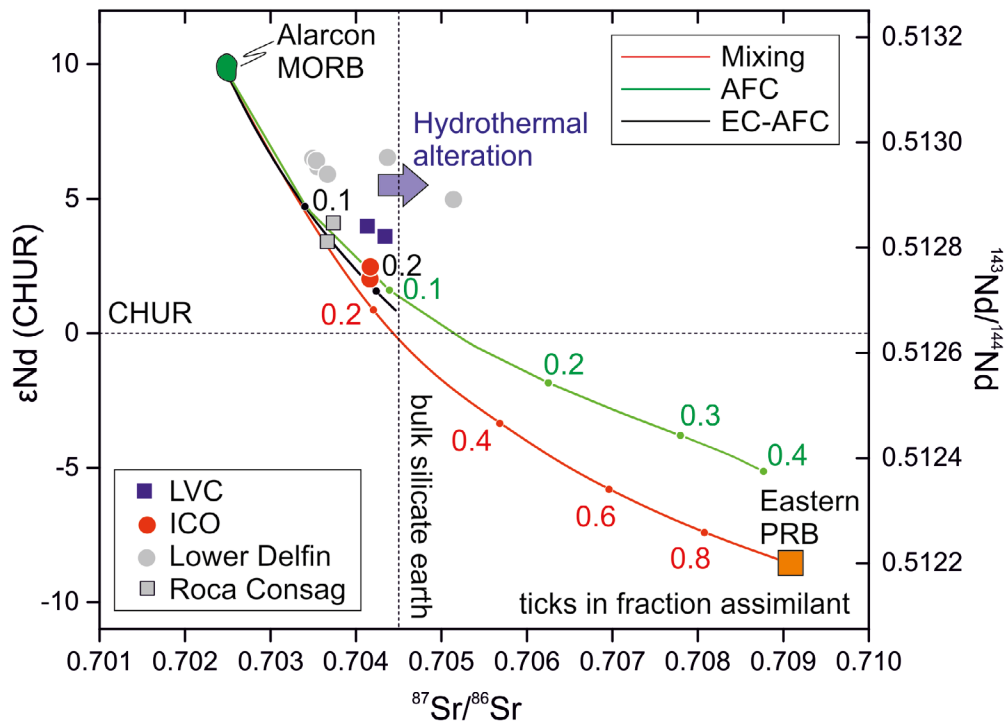Figure 10. Isotope variation diagram for whole rock $^{144}Nd/^{143}Nd$ (εNd) *vs.* $^{87}Sr/^{86}Sr$ compositions. Modelled mixing and assimilation-fractional crystallization (AFC) curves are indicated for parental MORB (Alarcón; εNd = +9.8; $^{87}Sr/^{86}Sr$ = 0.702476; Castillo *et al.*, 2002) and crustal contaminant typical of eastern Peninsular Ranges Batholith (εNd = -8.5; $^{87}Sr/^{86}Sr$ = 0.709; Herzig and Jacobs, 1994). Classical AFC curves are calculated for r (rate assimilation/crystallization) = 0.5 and bulk mineral-melt partitioning coefficients D(Nd) = 0.28 (Nd magma = 6.74 ppm; Nd assimilate 25.6 ppm) and D(Sr) = 1.6. (Sr magma = 203 ppm; Sr assimilate 289 ppm). Energy-constrained (EC) AFC curves use parameters as above and thermal conditions similar to Spera and Bohrson (2001) with an initial (liquidus) magma temperature of 1100°C. The assimilant initial and liquidus temperature were set at 600°C and 1100°C, respectively. Magma and assimilant heat capacities (enthalpies of fusion) were 1484 J·kg⁻¹·K⁻¹ (390 kJ·kg⁻¹) and 1370 J·kg⁻¹·K⁻¹ (270 kJ·kg⁻¹), respectively. All wall rock melt was mixed into the magma. Data from Lower Delfín andesite and rhyolite pumice from Martín-Barajas *et al.* (2008), data from Roca Consag is from Schmitt *et al.* (2013).

REFERENCES

Aragón-Arreola, M., Martín-Barajas, A., 2007, Westward migration of extension in the Northern Gulf of California: Geology, 2007; 35(6), 571-574.

Bottomley, J.R., York, D., 1976, ⁴⁰Ar-³⁹Ar age determinations on the Owyhee basalt of the Columbia Plateau: Earth and Planetary Science Letters; 31(1), 75-84.

Bouvier, A., Vervoort, D.J., Patchett, J., 2008, The Lu–Hf and Sm–Nd isotopic composition of CHUR: Constraints from unequilibrated chondrites and implications for the bulk composition of terrestrial planets: Earth and Planetary Science Letters, 273 (1-2), 48-57.

Castillo, R.P., Hawkins, W.J., Lonsdale, F.P., Hilton, D.R., Sahaw, MA., 2002, Petrology of Alarcon Rise lavas, Gulf of California: Nascent intracontinental

ocean crust: Journal of Geophysical Research, 107 (B10, 2222).

Castro, R.R., Stock, J.M., Hauksson, E., Clayton, R.W., 2017, Active tectonics in the Gulf of California and seismicity (M>3.0) for the period 2002–2014: Tectonophysics, 719-720, 4-16.

Cisneros de León, A., Schmitt, A.K., Storm, S., Weber, B., Schindlbeck-Belo, J.C., Trumbull, R.B., Juárez, F., 2019, Millennial to Decadal Magma Evolution in an Arc Volcano from Zircon and Tephra of the 2016 Santiaguito Eruption (Guatemala): Lithos, 340-341, 209-222.

De Paolo, J.D., 1981, Trace element and isotopic effects of combined wall-rock assimilation and fractional crystallization: Earth and Planetary Science Letters, 53 (2), 189-202.

Fletcher, M.J., Teran, J.O., Rockwell, K.T., Oskin, M., Hudnut, W.K., Mueller, J.K., *et al.*, 2014, Assembly of a large earthquake from a complex fault system: Surface rupture kinematics of the 4 April 2010 El Mayor–Cucapah (Mexico) Mw 7.2 earthquake: Geosphere 10 (10), 1-31.

Grimes, C.B., John, B.E., Kelemen, P.B., Mazdab, F.K., Wooden, J.L., Cheadle, M.J., Hanghøj, K., Schwartz, J.J., 2007, Trace element chemistry of zircons from oceanic crust: A method for distinguishing detrital zircon provenance: Geology, 35 (7), 643-646.

Heinonen, S.J., Kieran, A., Heinonen, A., Fred, R., Virtanen, J.V., Bohrson, A.W., Spera, J. F., 2021, From Binary Mixing to Magma Chamber Simulator: Geochemical Modeling of Assimilation in Magmatic Systems, *in* Massota, M., Beier, C., Mollo, S. (eds.), Crustal magmatic system evolution: Anatomy, Architecture, and Physico-Chemical Processes: American Geophysical Union, pp 151-178.

Henyey, T.L., Bischoff, J.L., 1973, Tectonic elements of the northern part of the Gulf of California: Geological Society of America Bulletin, 84, 315-330.

Herzig, C., Jacobs, C.D., 1994, Cenozoic volcanism and two-stage extension in the Salton trough, southern California and northern Baja California: Geology, 22 (11), 991-994.

Higa, J.T., Brown, N.D., Moon, S., Stock, J.M., Sabbeth, L., Bennett, S.E.K., Martín-Barajas, A., Argueta, M.O., 2022, Microcontinent Breakup and Links to Possible Plate Boundary Reorganization in the Northern Gulf of California, México: Tectonics, doi: 10.1029/2021TC006933

Hooper, P.R, Johnson, D.M., Conrey, R.M., 1993, Major and trace element analyses of rocks and minerals by automated x-ray spectrometry: Pullman, WA, USA, Washington State University, Geology Department, Open File Report, 12 pp.

Hurtado-Brito, 2012. El registro volcánico en las cuencas rift del norte del Golfo de California a partir de sísmica de reflexión: Centro de Investigación Científica y de Educación Superior de Ensenada, Earth Sciences master's science thesis, 100 pp.

Kuiper, K.F., Deino, A., Hilgen, F.J, Krijgsman, W., Renne P.R., Wijbrans, J.R., 2008. Synchronizing rock clocks of Earth history: Science, 320(5875), 500-4.

Le Bas, M. J., Le Maitre, R. W., Streckeisen, A., Zanettin, B., 1986, A chemical classification of volcanic rocks based on the total alkali-silica diagram: Journal of Petrology, 77, 24–37.

Lonsdale, P., 1989, Geology and tectonic history of the Gulf of California, *in* Winterer, D., Hussong, M., Decker, R.W. (eds.), The Eastern Pacific and Hawaii. The Geology of North America, N: Boulder, Colorado, Geological Society of America, 499-521.

Martin-Barajas, A., Weber, W., Schmitt, A.K., Lonsdale, P., 2008, Recent Rift Volcanism in the Northern Gulf of California and the Salton Through: Why a Preponderance of Evolved Magmas? American Geophysical Union Fall Meeting; San Francisco CA.

Martin-Barajas., A., González-Escobar, M., Fletcher, J.M., Pacheco, M., Oskin, M., Dorsey, R., 2013, Thick deltaic sedimentation and detachment faulting delay the onset of continental rupture in the Northern Gulf of California: Analysis of seismic reflection profiles: Tectonics, 32 (5), 1294-311.

Paz-Moreno, F.A., Demant, A., 1999, The recent Isla San Luis volcanic center: petrology of a rift-related volcanic suite in the northern Gulf of California, Mexico: Journal of Volcanology and Geothermal Research, 93, 31-52.

Pearce, N.J., Perkins W.T., Westgate, J.A., Gorton, M.P., Jackson S.E., Neal C.R., Chenery, S.P., 1997, A Compilation of New and Published Major and Trace Element Data for NIST SRM 610 and NIST SRM 612 Glass Reference Materials: Geostandards Newsletter, 21, 115-44.

Persaud, P., Stock, J.M., Steckler, M., Martín-Barajas, A., Diebold, J., González-Fernández, A., Mountain, G.S., 2003, Active deformation and shallow structure of the Wagner Consag, and Delfin Basins, northern Gulf of California, Mexico: Journal of Geophysical Research, 2003, 108 (B7), 2355, doi:10.1029/2002JB001937

Plattner, C., Malservisi, R., Dixon, T.H., LaFemina, P., Sella, G.F., Fletcher, J.M., Suárez-Vidal, F., 2007, New constraints on relative motion between the Pacific Plate and Baja California microplate (Mexico) from GPS measurements: Geophysical Journal International, 170 (3), 1373-1380.

Plattner, C., Malservisi, R., Amelung, F., Dixon, H.T., Hackl, M., Verdecchia, A., Lonsdale, P., Suarez-Vidal, F., Gonzalez-Garcia, J., 2015, Space geodetic observation of the deformation cycle across the Ballenas transform, Gulf of California: Journal of Geophysical Research, 120, 5843-5862.

Reid, M.R., Coath, C.D., Harrison, T.M., McKeegan, K.D., 1997: Earth and Planetary Science Letters, 150 (1-2), 27-39.

Roddick, J.C., 1983, High Precision intercalibration of $^{40}Ar/^{39}Ar$ standards: Geochimica and Cosmochimica Acta, 47, 887-898.

Sano, Y., Tsutsumi, Y., Terada, K., Kaneoka, I., 2002, Ion microprobe U–Pb dating of Quaternary zircon: implication for magma cooling and residence: Journal of Volcanology and Geothermal Research, 117, 285-26.

Schmitt, A.K., Vazquez, A.J., 2017, Secondary Ionization Mass Spectrometry Analysis in Petrochronology: Reviews in Mineralogy and Geochemistry, 2017, 83 (1), 199-230.

Schmitt, A.K., Groove, M., Harrison, T.M., Lovera, O., Hulen, J., Walters, M., 2003, The Geysers-Cobb Mountain Magma System, California (Part 1): U-Pb zircon ages of volcanic rocks, conditions of zircon crystallization and magma residence times: Geochimica and Cosmochimica Acta, 67(18), 3423-3442.

Schmitt, A.K., Chamberlain, K.R., Swapp, S.M., Harrison, T.M., 2010, In situ U-Pb dating of micro-baddeleyite by secondary ion mass spectrometry: Chemical Geology, 269 (3-4), 386-395.

Schmitt, A.K., Martín, A., Stockli, D., Farley, K.A., Lovera, O.M., 2013, (U-Th)/He zircon and archaeological ages for a late prehistoric eruption in the Salton Trough (California, USA): Geology, 2013, 41 (1), 7-10.

Seiler, C., Gleadow, A.J.W., Fletcher, J.M., Kohn, B.P., 2009, Thermal evolution of a sheared continental margin: Insights from the Ballenas transform in Baja California, Mexico: Earth and Planetary Science Letters, 285 (1-2), 61-74.

Spera, J.F., Bohrson, A.W., 2001. Energy-Constrained Open-System Magmatic Processes I: General Model and Energy-Constrained Assimilation and Fractional Crystallization (EC-AFC) Formulation: Journal of Petrology, 42(5), 999-1918.

Stacey, J.S., Kramers, J.D., 1975, Approximation of terrestrial lead isotope evolution by a two-stage model: Earth and Planetary Science Letters, 26(2), 207-221.

Steiger, R.H., Jager, E., 1977, Subcommission on geochronology; Convention on the use of decay constants in geo- and cosmochronology: Earth and Planetary Science Letters, 36, 359-362.

Stock, J., Martín-Barajas, A., Chapman, A., López-Martínez, M., 2009, Net slip across the Ballenas transform fault measured from offset ignimbrite deposits: EOS Trans American Geophysical Union Fall Meeting, Abstract Proceedings, 53.

Sun, S., McDonough, W.F., 1989, Chemical and isotopic systematics of oceanic basalts, in Sounders, A.D., Norry, M.J. (eds), Magmatism in the ocean basins: Geological Society, London, Special Publications, 42, 313-345.

Szymanowski, D., Fehr, A.M., Guillong, M., Coble, M., Wotzlawa, J.F., Nasdalac, L., Ellisa, S.B. Bachmanna, O., Schönbächlera, 2018, M. Isotope-dilution anchoring of zircon reference materials for accurate Ti-in-zircon thermometry: Chemical Geology, 481, 146-154.

Téllez-Velázquez, G., 2018, Estructura y evolución de las Cuencas Delfín Superior y Delfín Inferior: interpretación de perfiles de reflexión sísmica: Centro de Investigación Científica y de Educación Superior de Ensenada, Earth Sciences master's thesis, 74 pp.

Weber, B., Scherer, E.E., Martens, U.K., Mezger, K., 2012, Where did the Lower Paleozoic Rocks of Yucatan Come from? A U-Pb, Lu-Hf, and Sm-Nd Isotope Study: Chemical Geology, 312-313, 1-17.

Wiedenbeck, M., Hanchar, J., Peck, W., Sylvester, P., Valley, J., Whitehouse, M., Kronz, A., Morishita, Y., Nasdala, L., Fiebig, J., Franchi, I., Girard, J.-P., Greenwood, R.C., Hinton, R., Kita, N., Mason, P.R.D., Norman, M., Ogasawara, M., Piccoli, P.M., Rhede, D., Satoh, H., Schulz-Dobrick, B., Skår, O., Spicuzza, M.J., Terada, K., Tindle, A., Togashi, S., Vennemann, T., Xie, Q., Zheng, Y.-F., 2004, Further characterization of the 91500 zircon crystal: Geostandards and Geoanalytical Research, 28, 9-39.

Erratum / *Fe de erratas*

Erratum to
Pleistocene volcanism along the margins of the
Canal de Ballenas transform fault, Gulf of California

published in /*publicado en*
Revista Mexicana de Ciencias Geológicas, 39(1), 2022

by / *por*
**Arturo Martín-Barajas[1,*], Axel K. Schmitt[2], Bodo Weber[1], and
Margarita López-Martínez[1]**

[1] *Departamento de Geología, Centro de Investigación Científica y Educación Superior de Ensenada, Baja California, Mexico.*
[2] *Institute of Earth Sciences, Ruprecht-Karls-Universität, Heidelberg, Germany.*
*amartin@cicese.mx

In the above article, the data of the reference:
En el artículo indicado arriba los datos de la referencia:

Schmitt, A.K., Martín, A., Stockli, D., Farley, K.A., Lovera, O.M., 2013, (U-Th)/He zircon and archaeological ages for a late prehistoric eruption in the Salton Trough (California, USA): Geology, 2013, 41 (1), 7-10.

Are not correct, they must be:
No son correctos y en su lugar deben ser:

Schmitt, A.K., Martín, A., Weber, B., Stockli, D.F., Zou, H., Shen, C.C., 2013, Ocean magmatism in sedimentary basins of the northern Gulf of California rift: Geological Society of America Bulletin, 125(11-12), 1833-1850.

In-text citations to these authors remain unchanged.
Las citas a estos autores en el texto permanecen sin cambio.

This erratum has been attached to the online version of the paper on april 8th, 2022. The editors apologize for this mistake.
Esta errata ha sido anexada a la versión electrónica del artículo el 8 de abril de 2022. Los editores lamentan este error.

Artículo original: *DOI: http://dx.doi.org/10.22201/cgeo.20072902e.2022.1.1659*

Martín-Barajas, A., Schmitt, A.K., Weber, B., López-Martínez, M., EN PRENSA, Erratum to Pleistocene volcanism along the margins of the Canal de Ballenas transform fault, Gulf of California: Revista Mexicana de Ciencias Geológicas, v. XX, núm. X, p. XXX-XXX.

DOI: http://dx.doi.org/10.22201/cgeo.20072902e.2022.2._____

1